

# REPORT DOCUMENTATION PAGE

Form Approved  
OMB No. 0704-0188

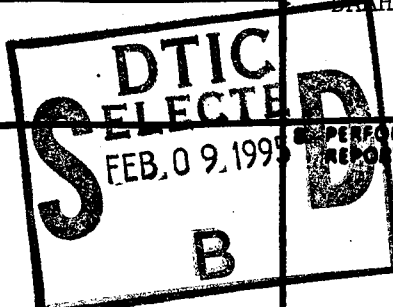
Public reporting burden for this collection of information is estimated to average 1 hour per response, including the time for reviewing instructions, searching existing data sources, gathering and maintaining the data needed, and completing and reviewing the collection of information. Send comments regarding this burden estimate or any other aspect of this collection of information, including suggestions for reducing this burden, to Washington Headquarters Services, Directorate for Information Operations and Reports, 1215 Jefferson Davis Highway, Suite 1204 Arlington, VA 22202-4302, and to the Office of Management and Budget, Paperwork Reduction Project (0704-0188) Washington, DC 20503.

1. AGENCY USE ONLY (Leave blank) 2. REPORT DATE 10/27/94 3. REPORT TYPE AND DATES COVERED Final Report, 9/1/93 - 8/31/94

4. TITLE AND SUBTITLE High Performance Electromagnetic Simulation Tools 5. FUNDING NUMBERS DAAH04-93-G-0453

6. AUTHOR(S) Stephen D. Gedney Keith W. Whites

7. PERFORMING ORGANIZATION NAME(S) AND ADDRESS(ES) Department of Electrical Engineering University of Kentucky 453 Anderson Hall Lexington, KY 40506-0046 8. PERFORMING ORGANIZATION REPORT NUMBER



9. SPONSORING/MONITORING AGENCY NAME(S) AND ADDRESS(ES) U.S. Army Research Office P. O. Box 12211 Research Triangle Park, NC 27709-2211 10. SPONSORING/MONITORING AGENCY REPORT NUMBER ARO 32378.1-EL-DPS

11. SUPPLEMENTARY NOTES The views, opinions and/or findings contained in this report are those of the author(s) and should not be construed as an official Department of the Army position, policy, or decision, unless so designated by other documentation.

12a. DISTRIBUTION/AVAILABILITY STATEMENT Approved for public release; distribution unlimited. 12b. DISTRIBUTION CODE

**TRACT (Maximum 200 words)**

Army Research Office Grant # DAAH04-93-G-0453 has supported the purchase of 24 additional compute nodes that were installed in the Intel iPSC/860 hypercube at the University of Kentucky (UK), rendering a 32-node multiprocessor computer. This facility has allowed the investigators to explore and extend the boundaries of electromagnetic simulation for important areas of Defense concerns including microwave monolithic integrated circuit (MMIC) design/analysis and electromagnetic materials research and development. The iPSC/860 has provided an ideal platform for MMIC circuit simulations. A number of parallel methods based on direct time-domain solutions of Maxwell's equations have been developed on the iPSC/860, including a parallel finite-difference time-domain (FDTD) algorithm, and a parallel planar generalized Yee-algorithm (PGY). The iPSC/860 has also provided an ideal platform on which to develop a "virtual laboratory" to numerically analyze, scientifically study and develop new types of materials with beneficial electromagnetic properties. These materials simulations are capable of assembling hundreds of microscopic inclusions from which an electromagnetic full-wave solution will be obtained *in toto*. This powerful simulation tool has enabled research of the full-wave analysis of complex multicomponent MMIC devices and the electromagnetic properties of many types of materials to be performed numerically rather than strictly in the laboratory.

19950203 213

14. SUBJECT TERMS iPSC/860 hypercube, MMIC, parallel algorithms, FDTD, PGY, materials characterization, chiral media, bianisotropic 15. NUMBER OF PAGES 34 16. PRICE CODE 17. SECURITY CLASSIFICATION OF REPORT UNCLASSIFIED 18. SECURITY CLASSIFICATION OF THIS PAGE UNCLASSIFIED 19. SECURITY CLASSIFICATION OF ABSTRACT UNCLASSIFIED 20. LIMITATION OF ABSTRACT UL

***HIGH PERFORMANCE ELECTROMAGNETIC  
SIMULATION TOOLS***

**FINAL REPORT**

**STEPHEN D. GEDNEY AND KEITH W. WHITES**

**OCTOBER 27, 1994**

**U.S. ARMY RESEARCH OFFICE**

**GRANT # DAAHO4-93-G-0453**

**DEPARTMENT OF ELECTRICAL ENGINEERING  
UNIVERSITY OF KENTUCKY**

**APPROVED FOR PUBLIC RELEASE**

**DISTRIBUTION UNLIMITED**

# TABLE OF CONTENTS

<b>SECTION</b>	<b>PAGE</b>
<b>1. STATEMENT OF PROBLEMS STUDIED</b> .....	1
<b>2. SUMMARY OF RESULTS</b> .....	2
<b>2.1 INTRODUCTION</b> .....	5
<b>2.2. FULL WAVE ANALYSIS OF MICROWAVE MONOLITHIC INTEGRATED         CIRCUITS - S. GEDNEY</b> .....	4
2.2.1 <i>Parallel FDTD Algorithm</i> .....	4
2.2.1 <i>Parallel PGY Algorithm</i> .....	5
2.2.3 <i>Results</i> .....	11
2.2.4 <i>References</i> .....	17
<b>2.3. ELECTROMAGNETIC PROPERTIES OF MATERIALS         - K. W. WHITES</b> .....	18
2.3.1 <i>Solution Methodology</i> .....	18
2.3.2 <i>Results</i> .....	21
2.3.2.a <i>Partial Verification of the Material Model Method</i> .....	21
2.3.2.b <i>Free space host, lossless inclusions results</i> .....	23
2.3.2.c <i>Lossless host and inclusions results</i> .....	26
2.3.2.d <i>Lossy host, lossless inclusions results</i> .....	26
2.3.2.e <i>Free-space host, lossy inclusions results</i> .....	28
2.3.3 <i>References</i> .....	30
<b>3. PUBLICATIONS</b> .....	31
<b>3.1 JOURNAL PAPERS PUBLISHED/SUBMITTED</b> .....	31
3.1.1 <i>S. Gedney</i> .....	31
3.1.2 <i>K. Whites</i> .....	31
<b>3.1 CONFERENCE PAPERS PUBLISHED/PRESENTED</b> .....	31
3.2.1 <i>S. Gedney</i> .....	31
3.2.2 <i>K. Whites</i> .....	32
<b>4. SUPPORTING PERSONNEL</b> .....	32
<b>5. REPORT OF INVENTIONS</b> .....	32

# 1. STATEMENT OF PROBLEMS STUDIED

Army Research Office Grant # DAAHO4-93-G-0453 has supported the purchase of 24 additional compute nodes that were installed in the Intel iPSC/860 hypercube at the University of Kentucky (UK). This has resulted in a 32-node iPSC/860, providing nearly a GFLOPS of computing power, 512 MB of core memory and 6 GB of concurrent I/O. This facility has allowed the investigators to explore and extend the boundaries of electromagnetic simulation for important areas of Defense concerns including microwave monolithic integrated circuit (MMIC) design/analysis and electromagnetic materials research and development.

The 32-node iPSC/860 hypercube has provided an ideal platform for MMIC circuit simulations. A number of parallel methods based on direct time-domain solutions of Maxwell's equations have been developed on the iPSC/860, including a parallel finite-difference time-domain (FDTD) algorithm, and a parallel planar generalized Yee-algorithm (PGY). With the development of these techniques, this powerful platform has enabled the full-wave analysis of complex multicomponent MMIC devices for a number of applications.

The iPSC/860 has also provided an ideal platform on which to develop a "virtual laboratory" to numerically analyze, scientifically study and develop new types of materials with beneficial electromagnetic properties. These materials simulations are capable of assembling hundreds of microscopic inclusions from which an electromagnetic full-wave solution will be obtained *in toto*. For sparse distributions of inclusions, this numerical laboratory is able to accommodate literally thousands of inclusions. This powerful simulation tool has enabled research into the electromagnetic properties of many types of materials to be performed numerically rather than strictly in the laboratory.

<b>Accession For</b>	
NTIS GRA&I	<input checked="" type="checkbox"/>
DTIC TAB	<input type="checkbox"/>
Unannounced	<input type="checkbox"/>
Justification	
By	
Distribution	
Availability Codes	
Dist	Avail and/or Special
A-1	

## 2. SUMMARY OF RESULTS

### 2.1 INTRODUCTION

The 32-node iPSC/860 hypercube has provided a high performance simulation platform that has significantly benefited two distinct research projects currently ongoing at the University of Kentucky: 1) The full-wave analysis of microwave monolithic integrated circuits (MMICs), and 2) electromagnetic materials research and development.

In the last decade, MMICs have played a leading role in the design of microwave communications systems. As the fabrication technologies of these devices have matured, both military and commercial applications have demanded smaller and denser MMICs operating over larger bandwidths and at higher operating frequencies (into the  $K_a$  and  $U$  bands). This has led to an increased need for more rigorous analyses that explicitly model the electromagnetic interactions within these devices. Although, it is instructive to isolate each element of the MMIC and analyze them independently, proper characterization of densely packaged circuits require the rigorous analysis of entire circuits simultaneously, or large blocks of circuits. To this end, coupling between devices that can significantly perturb the circuit operation can be accounted for.

The objective of this research has been to complete the development of a MMIC circuit simulator based on a direct time-domain solution of Maxwell's equations and parallel algorithms. The simulator is capable of analyzing MMICs using either the traditional finite-difference time-domain (FDTD) method or the robust planar generalized Yee-algorithm (PGY). The simulator is capable of analyzing passive devices with lumped loads, as well as active (nonlinear) devices. To model highly complex circuits using the generalized Yee-algorithm, the simulator has been interfaced with the computer aided design (CAD) system SDRC IDEAS for modeling the circuits and performing the mesh generation for its discrete representation and a graphics package for visualization and analysis of results. With this potential, models consisting of upwards to  $80 \times 10^6$  degrees of freedom have been analyzed using the FDTD algorithm (on a regular grid), and upwards to  $60 \times 10^6$  degrees of freedom have been analyzed using the PGY algorithm on the 32-node iPSC/860. This has provided a powerful computational laboratory and has facilitated ongoing research of the design and development of MMIC circuits for microwave communications in the upper GHz frequency bands.

The second area of focus for this high performance simulation platform is one of today's most dynamic areas of physical science — materials research. Using sophisticated manufacturing techniques and the availability of new types of molecules, it is possible to build new exotic materials having unusual properties. The additional compute nodes which have expanded the University of Kentucky Intel iPSC/860 have been used for numerically constructing a "virtual laboratory" in which the electromagnetic properties of new types of materials have been

investigated. Currently, an ongoing research program is focusing on the determination of the macroscopic constitutive parameters for an interesting class of substance called chiral materials. The modifier "chiral," from the Greek word meaning handed, refers to the nature of the inclusions which constitute the material at the microscopic level. The impetus for this research is that on the macroscopic level, these materials have been shown to provide unusual and sometimes very beneficial behavior in such applications as radar absorbent materials and guided-wave applications. For wave absorption, understanding and modeling the interactions of the inclusions, the host material and the incident wave at the *microscopic* level is necessary to both develop a macroscopic model as well as to design and optimize this behavior.

In macroscopic chiral studies which have appeared in the literature, the constitutive parameters describing the macroscopic behavior of the chiral substance are assumed known from which parametric studies are performed. In reality these parameters are not known and to the author's knowledge no other comprehensive treatment has been given to their determination. Using numerical simulations, a technique to compute these constitutive parameters for effectively chiral materials has been developed and results indicate that such a procedure is attainable. As would be expected such a numerical simulation is very costly in terms of computational resources. Additionally, this research program seeks to analyze other types of materials, not only chiral. With this in mind, the algorithms and procedures which have been developed were designed with this generality in focus.

## 2.2. FULL WAVE ANALYSIS OF MICROWAVE MONOLITHIC INTEGRATED CIRCUITS - S. GEDNEY

### 2.2.1 Parallel FDTD Algorithm

The FDTD method is based on the discretization of Maxwell's curl equations

$$-\mu \frac{\partial \vec{H}}{\partial t} = \nabla \times \vec{E} \quad (2.1a)$$

$$\epsilon \frac{\partial \vec{E}}{\partial t} + \sigma \vec{E} = \nabla \times \vec{H} \quad (2.1b)$$

using central difference approximations of time and spatial derivatives. To this end, the vector fields are projected onto the edges of a regular orthogonal dual, staggered grid. Based on this discretization, the curl equations can be expressed in a discrete form as [1]

$$\vec{H}^{n+1/2} = \vec{H}^{n-1/2} + A_h \vec{E}^n \quad (2.2)$$

$$\vec{E}^{n+1} = D_e \vec{E}^n + A_e \vec{H}^{n+1/2} \quad (2.3)$$

where  $\vec{H}$  and  $\vec{E}$  are vectors of coefficients representing the vector field intensities on the grid edges, the superscript  $n$  represents the time increment,  $D_e$  is a diagonal matrix, and  $A_e$  and  $A_h$  are sparse matrices. The entries of these matrices are found in [1]. Equations (2.2) and (2.3) provide an explicit time-marching solution for the electric and magnetic field intensities within the discrete volume. By staggering the electric and magnetic fields in both space and time, the solution is second-order accurate in both space and time (assuming uniform grids) providing the time step satisfies the stability criterion

$$\Delta t < \frac{1}{c_0 \sqrt{\frac{1}{\Delta x^2} + \frac{1}{\Delta y^2} + \frac{1}{\Delta z^2}}} \quad (2.4)$$

The FDTD algorithm has the principle advantage that since the grid is regular and orthogonal,  $D_e$ ,  $A_e$  and  $A_h$  are regular and never need be stored explicitly, but are easily computed each iteration. This results in an extremely memory efficient algorithm.

The parallel FDTD algorithm is based on a spatial decomposition of the regular grid structure. To this end, the original domain is spatially decomposed into contiguous sub-domains which are rectangular in shape, non-overlapping, sharing common surfaces only, and are of equal size (see Fig. 2.1). The boundaries, or surfaces, shared by sub-domains are chosen by taking slices along edges of the primary grid. Each subdomain is then mapped onto independent processors. Due to the regularity of the grid, the work load is easily balanced between processors.

Figure 2.1 illustrates the shared surface between two contiguous sub-domains with a shared surface in an  $x = \text{constant}$  plane. The arrows represent the tangential electric fields on the shared surface, and the dots represent the normal magnetic field vectors. The tangential electric fields

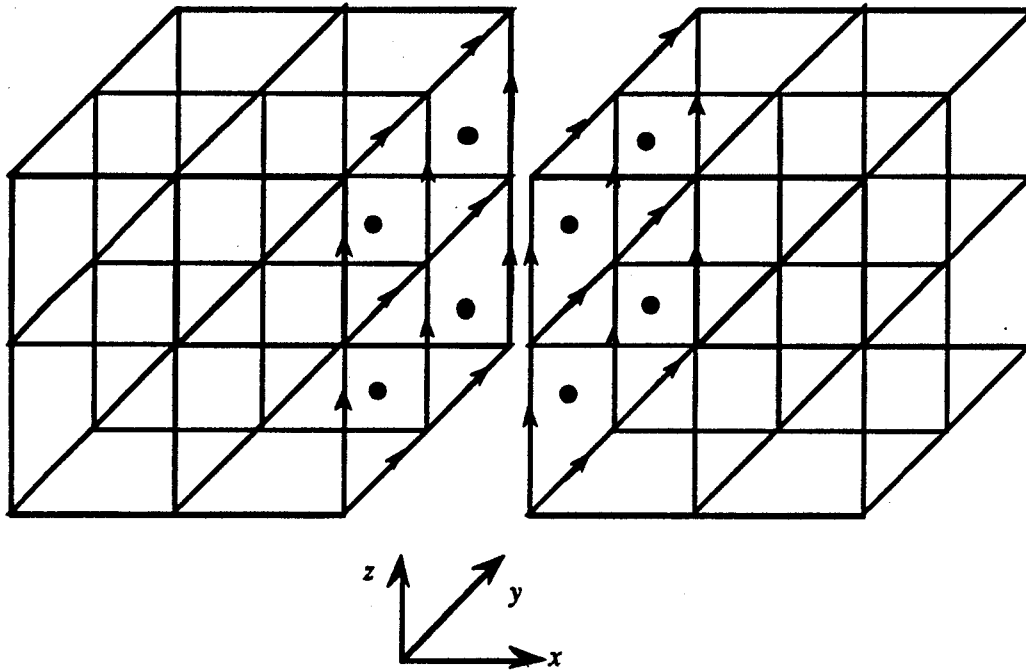


Fig. 2.1. Shared interface between two sub-domains along the y-z plane. The arrows represent the shared electric field vectors tangential to the shared boundary and the dots represent the normal magnetic field vectors normal to the shared boundary.

$e_{y_{i,j+1/2}}^{n+1/2}$  and  $e_{z_{i,j+1/2}}^{n+1/2}$  are updated using (2.3) and is dependent on the magnetic field vectors normal to the four faces sharing these edges. However, each processor has at most three of the four faces needed to update the electric field in local memory, and it becomes necessary to retrieve the needed data from adjacent processors.

The magnetic field vectors normal to the shared interface are updated using (2.2). The update of the magnetic field passing through a face is proportional to the curl of the electric field about the edges bounding the face. Since each processor has the updated value of the tangential electric fields on the shared interface, the normal magnetic field can be updated independently on each processor. Therefore, interprocessor communication is not needed when updating the magnetic fields within each sub-domain. Rather, it is much more expedient to simply update the normal magnetic fields in the shared boundary redundantly on each processor sharing the face.

### 2.2.1 Parallel PGY Algorithm

The PGY algorithm is based on the discretization of Ampere's and Faraday's laws in their integral form [2, 3] by projecting the vector fields onto the edges of a dual, staggered grid. Unlike the FDTD algorithm, the grid is assumed to be unstructured and irregular. The PGY algorithm is specifically applied to structures which have *planar* symmetry, namely three-dimensional geometries that can be uniquely described by a projection onto a two-dimensional plane. For

example a microstrip circuit printed on a planar dielectric substrate backed by a ground plane (not necessarily infinite) can be said to have planar symmetry. By exploiting this symmetry, the three-dimensional grid can then be described by a two-dimensional grid which is extruded into the third-dimension in a regular sense [2]. The principal advantage of this assumption is that only the two-dimensional grid need be stored, and the update matrices, similar to (2.2) and (2.3), need only be stored for one layer of cells. This leads to a tremendous savings in memory overhead. Finally, the method is fully explicit and has been shown to be a highly scalable algorithm [2, 3].

The planar generalized Yee-algorithm is based on a direct solution of the time-dependent Maxwell's equations in their integral form. The electric and magnetic field intensities are initially normalized as

$$\begin{aligned}\bar{e} &= \vec{E} / \sqrt{\eta_0} \\ \bar{h} &= \vec{H} \sqrt{\eta_0}\end{aligned}\tag{2.5}$$

where  $\eta_0$  is the characteristic wave impedance in free space. Faraday's law and Ampère's law are then expressed in their integral form as

$$\oint_c \bar{e} \cdot d\bar{\ell} = -\frac{1}{c_0} \frac{\partial}{\partial t} \iint_s \mu_r \bar{h} \cdot d\bar{S}\tag{2.6}$$

$$\oint_c \bar{h} \cdot d\bar{\ell} = \frac{1}{c_0} \frac{\partial}{\partial t} \iint_s \epsilon_r \bar{e} \cdot d\bar{S} + \eta_0 \iint_s \sigma \bar{e} \cdot d\bar{S}\tag{2.7}$$

where  $c_0$  is the free space velocity of light,  $\mu_r$  and  $\epsilon_r$  are the relative permeability and permittivity, respectively, and  $\sigma$  is the absolute conductivity. The principle advantage of this normalization is that the magnitudes of  $\bar{e}$  and  $\bar{h}$  will be of the same order, reducing rounding error. Furthermore, it is much more convenient to work with the relative permittivity and permeabilities rather than their absolute values.

Faraday's and Ampère's laws are expressed in a discrete form by mapping  $\bar{e}$  and  $\bar{h}$  into a discrete three-dimensional space. The mapping consists of projecting the vector fields onto the edges of a dual grid, composed of two staggered grids, referred to as the primary and secondary grids. Each grid is a three-dimensional grid that is described as being regular along the vertical direction (assumed to be the z-direction), and is unstructured in the horizontal direction. Conceptually, this grid can be generated by extruding a two-dimensional unstructured grid in the vertical direction, and segmenting it at discrete heights, as illustrated in Fig. 2.2. The secondary grid is staggered within the primary grid such that its vertices lie at the centroids of the primary grid cells, and the edges of the secondary grid connect the centroids by passing through the faces of the primary grid.

The electric and magnetic fields are then decomposed into orthogonal components

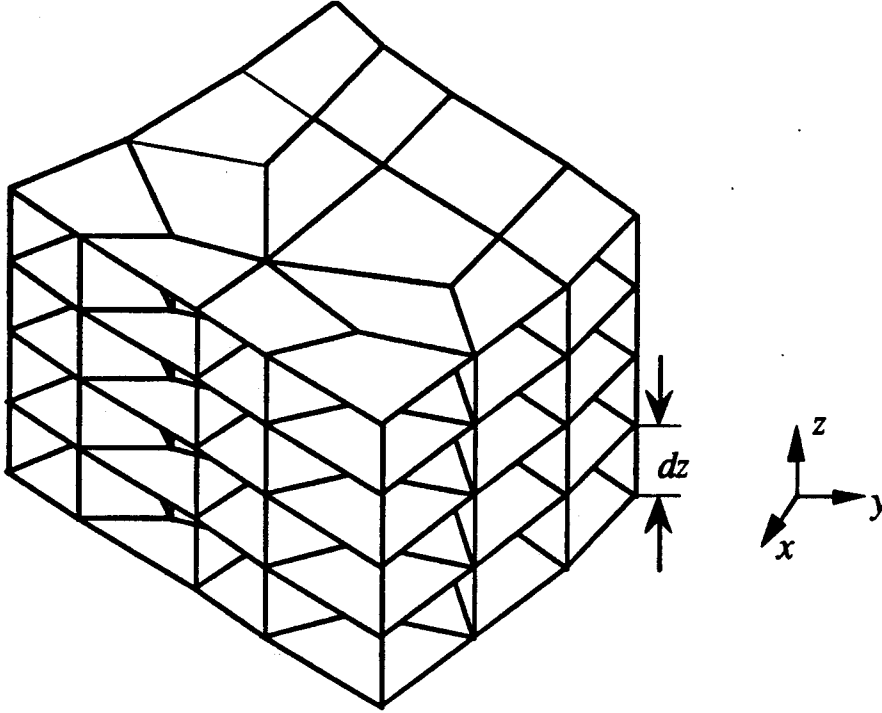


Fig. 2.2 An example of the primary grid described by similar two-dimensional unstructured grids cascated in the vertical  $z$ -direction in a regular sense.

$$\bar{e} = \bar{e}_i + \hat{z}e_z,$$

$$\bar{h} = \bar{h}_i + \hat{z}h_z. \quad (2.8)$$

Subsequently, the transverse electric and magnetic fields are mapped onto the horizontal edges of the primary and secondary grids, respectively. Likewise, the vertical electric and magnetic fields are mapped onto the vertical edges of the primary and secondary grids, respectively. The vector fields are assumed to be constant along their respective edge lengths, as well as over the dual face through which they pass.

Based on the above discretization, Faraday's and Ampère's laws are then mapped into the discrete space. The time derivative is then approximated using a central difference expression, which is second-order accurate if the fields are staggered in time. This leads to [2]

$$h_{z_j}^{n+1}(k) = h_{z_j}^n(k) - \frac{c_o dt}{A_p} \frac{1}{\mu_r(k)} \left[ \sum_{i=1}^{N_{rj}} e_{i_i}^{n+\frac{1}{2}}(k) \ell_i \right] \quad (2.9)$$

$$b_{i_i}^{n+1}(k + \frac{1}{2}) = b_{i_i}^n(k + \frac{1}{2}) - \frac{c_o dt}{dz |\ell_{i_i}|} \left[ \left( e_{z_m}^{n+\frac{1}{2}}(k + \frac{1}{2}) - e_{z_{m+1}}^{n+\frac{1}{2}}(k + \frac{1}{2}) \right) dz + \left( e_{i_i}^{n+\frac{1}{2}}(k+1) - e_{i_i}^{n+\frac{1}{2}}(k) \right) \ell_i \right] \quad (2.10)$$

$$e_{z_m}^{n+\frac{3}{2}}(k+\frac{1}{2}) = \left[ \left( \frac{\epsilon_{r_m}(k+\frac{1}{2})}{c_o \Delta t} \frac{\sigma_m(k+\frac{1}{2})\eta_o}{2} \right) e_{z_m}^{n+\frac{1}{2}}(k+\frac{1}{2}) - \frac{1}{A_s} \left[ \sum_{i=1}^{N_{sj}} h_{i_i}^{n+1}(k+\frac{1}{2}) \ell_i \right] \right] \frac{1}{\left( \frac{\epsilon_{r_m}(k+\frac{1}{2})}{c_o \Delta t} + \frac{\sigma_m(k+\frac{1}{2})\eta_o}{2} \right)} \quad (2.11)$$

$$d_{i_i}^{n+\frac{3}{2}}(k) = \frac{1}{\left( \frac{1}{c_o \Delta t} + \frac{\sigma_i(k+\frac{1}{2})\eta_o}{2\epsilon_{r_i}(k+\frac{1}{2})} \right)} \left[ \left( \frac{1}{c_o \Delta t} \frac{\sigma_i(k+\frac{1}{2})\eta_o}{2\epsilon_{r_i}(k+\frac{1}{2})} \right) d_{i_i}^{n+\frac{1}{2}}(k) - \frac{1}{dz \ell_i} \cdot \left[ \left( h_{z_j}(k) - h_{z_{j+1}}(k) \right) dz + \left( h_{i_i}^{n+1}(k-\frac{1}{2}) - h_{i_i}^{n+1}(k+\frac{1}{2}) \right) \ell_i \right] \right] \quad (2.12)$$

where  $d_t$  and  $b_t$  are the flux densities in the transverse plane,  $\Delta t$  is the time increment,  $n$  is the time index,  $k$  is the index along  $z$ ,  $A_p$  and  $A_s$  are the areas of the primary and secondary grid faces, respectively,  $N_{pi}$  and  $N_{sj}$  are the number of edges bounding the  $i$ -th primary and the  $j$ -th secondary grid faces, respectively, and the  $\ell_i$  are the length vectors of the primary or secondary grid edges. The material parameters  $\epsilon_r$ ,  $\mu_r$  and  $\sigma$  are assumed to be piecewise homogeneous in both the  $z$ -direction as well as in the transverse direction. At the interface of two unlike medium, the parameters are assigned an average value, as described in Appendix A of [4].

Based on (2.6) and (2.7), it is recognized that the flux densities updated in (2.10) and (2.11) are normal to the faces. However, the corresponding field intensities on the dual edges passing through these faces are not necessarily normal to the faces. As a result, the flux densities must be projected onto the edges before the dual fields can be updated. Since only one component of the field is locally known, an auxiliary operator must be introduced to perform the projection. To this end, the projection operators implemented in [4] are used to project the fields onto the dual edge passing through the face.

Let  $\vec{N}_p$  be the normal area vector to a primary grid transverse face, and  $\hat{s}$  be the unit vector along the dual grid edge passing through the face (Fig. 2.3). Using (2.10) the magnetic flux densities projected onto the normals of all the primary grid transverse faces are updated. Subsequently, for each face, a general flux density vector  $\vec{b}$  is introduced. From (2.10),  $\vec{b} \cdot \vec{N}_p$  is known at each edge. In Fig. 2.3, the edge identified is bound by vertices 1 and 2, which is identified by the index  $i = 1, 2$ . Each vertex is also shared by two additional edges which share a common cell. Let  $j$  represent one of these edges, where  $j = 1, 2$ . The normal area vector to the  $j$ -th edge associated with the  $i$ -th vertex is  $\vec{N}_{D_{i,j}}$ . Subsequently, we define a general flux density vector  $\vec{b}_{i,j}$  to be the local estimate of the magnetic flux vector associated with the  $i$ -th vertex and the  $j$ -th edge, where  $\vec{b}_{i,j}$  is computed by solving the two-dimensional system of equations

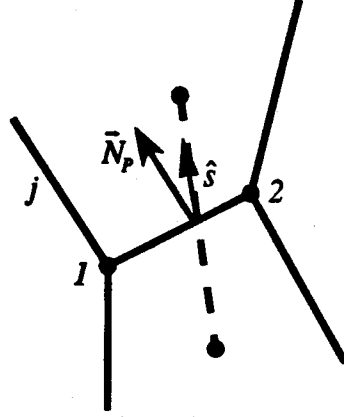


Fig. 2.3 Normal to a transverse primary face, and a dual edge passing through the face.

$$\begin{aligned}\bar{b}_{i,j} \cdot \bar{N}_D &= \bar{b} \cdot \bar{N}_D \\ \bar{b}_{i,j} \cdot \bar{N}_{D_{i,j}} &= \bar{b} \cdot \bar{N}_{D_{i,j}}\end{aligned}\quad (2.13)$$

where the right-hand-side is known from (2.10). Subsequently, introducing the weighting coefficient  $w_{i,j} = |\hat{z} \cdot (\bar{N}_D \times \bar{N}_{D_{i,j}})|$ , the flux density projected onto the dual edge is expressed as

$$\bar{b} \cdot \hat{s} = \frac{\sum_{i=1}^2 \sum_{j=1}^2 w_{i,j} (\bar{b}_{i,j} \cdot \hat{s})}{\sum_{i=1}^2 \sum_{j=1}^2 w_{i,j}}. \quad (2.14)$$

The field updates are then computed using (2.10)-(2.14). However, it is realized that computing the parameters for these equations requires a significant number of floating point operations, leading to a highly inefficient algorithm. However, by employing standard finite-element type techniques, the computational efficiency can be greatly enhanced by treating these linear operators as sparse matrices. To this end, (2.10)-(2.14) can be expressed in reduced form as

$$[H_z^{n+1}]_k = [H_z^n]_k + \bar{A}_h [E_t^{n+1/2}]_k \quad (2.15)$$

$$[B_t^{n+1}]_{k+1/2} = [B_t^n]_{k+1/2} + \bar{A}_h \begin{bmatrix} E_{z_{k+1/2}}^{n+1/2} \\ E_{t_{k+1}}^{n+1/2} \end{bmatrix} \quad (2.16)$$

$$[H_t^{n+1}]_{k+1/2} = \bar{A}_h [B_t^{n+1}]_{k+1/2} \quad (2.17)$$

$$[E_z^{n+3/2}]_{k+1/2} = \bar{D}_e [E_z^{n+1/2}]_{k+1/2} + \bar{A}_e [H_t^{n+1}]_{k+1/2} \quad (2.18)$$

$$[D_t^{n+3/2}]_k = \bar{D}_e [D_t^{n+1/2}]_k + \bar{A}_e \begin{bmatrix} H_{z_{k+1}}^{n+1} \\ H_{t_{k+1/2}}^{n+1} \end{bmatrix} \quad (2.19)$$

$$[E_i^{n+3/2}]_k = \overline{A}_i [D_i^{n+3/2}]_k \quad (2.20)$$

where the subscript  $k$  refers to the discrete height along the  $z$ -direction,  $D_i$  and  $B_i$  are the flux densities, the  $\overline{D}$ 's are diagonal matrices, and the  $\overline{A}$ 's are sparse matrices. Note that these matrices are only associated with the two-dimensional grid since they are the same for all values of  $k$  (inhomogeneities in material parameters are easily built into these expressions). As a result, the additional memory required to store these matrices is nominal.

Finally, the field updates are performed using (2.15)-(2.20), providing an extremely efficient computational technique that is second-order accurate for the simulation of the time-varying fields. Furthermore, the solution is stable, providing [4]

$$\Delta t < \frac{1}{c_o \sqrt{\left(\frac{1}{\Delta z}\right)^2 + 2\left(\frac{1}{\ell_{\min}}\right)^2}} \quad (2.21)$$

where  $\ell_{\min}$  is the minimum edge length in the model.

Once the matrices are computed, the field updates reduce to a series of sparse-matrix – vector multiplications, which is readily parallelizable. The parallel PGY algorithm is based on a spatial decomposition of the three-dimensional grid into contiguous, non-overlapping subdomains. This spatial decomposition, or partitioning, of the three-dimensional unstructured mesh is being performed by first partitioning the two-dimensional unstructured mesh using the Recursive Inertia Partitioning (RIP) algorithm [5] and a Greedy algorithm [6], and then using a trivial partitioning scheme along the regular dimension of the grid which is similar to the FDTD partition.

Once the mesh is decomposed into subdomains, a single subdomain is assigned to each processor. The matrices in (4) are then expressed as a subassembly of matrices, where each sub matrix represents the updates of the fields within each subdomain. Subsequently, the matrix-vector products on each processor are computed as

$$\overline{A}_i x_i = \overline{A}_i^{\text{int}} x_i + \sum_{j=1}^{N_{\text{shared}}} \left( \overline{A}_{i,j}^{\text{shared}} x_i \right) + \sum_{j=1}^{N_{\text{shared}}} R_x \left( \overline{A}_{j,i}^{\text{shared}} x_j \right) \quad (2.22)$$

where  $\overline{A}_i^{\text{int}}$  are the entries of  $\overline{A}_i$  associated with all field vectors internal to the  $i$ -th processor's subdomain,  $\overline{A}_{i,j}^{\text{shared}}$  are the entries of  $\overline{A}_i$  associated with all field vectors in the  $i$ -th processor's subdomain that lie on the boundary shared with the  $j$ -th domain,  $N_{\text{shared}}$  is the number of processors that share boundaries with the  $i$ -th processor, and  $R_x$  is the receive operator, receiving the vector of data from the  $j$ -th processor. The first two expressions on the right-hand-side of (2.22) are done completely in parallel on each processor, and the final term requires interprocessor communication. If the subdomains are equal in size, then the work load required to perform the matrix-vector products will be well balanced. If the number of edges shared by sub domains are

minimized, the lengths of the interprocessor communications will be minimal (note that the number of sub domains that each sub domain has interfaces with should be minimized as well). Furthermore, due to the regularity of the grid, the matrix vector multiplications It was shown in [3] that this leads to a highly efficient parallel algorithm.

### 2.2.3 Results

The parallel algorithms have been implemented in FORTRAN on the 32-node iPSC/860 hypercube. Care has been taken to optimize the codes for floating point and memory efficiency. For example vectorization is exploited in the inner loops of the computationally intensive tasks for each algorithm. Furthermore, full optimization was utilized when compiling the programs.

In each of the algorithms, unbounded media are modeled through the use of an absorbing boundary condition. The second-order dispersive boundary condition [7] was implemented to update the tangential fields on the exterior truncation boundary.

The expected storage requirements and the number of floating point operations required for each algorithm is presented in Table 2.1. In this table,  $N_x$ ,  $N_y$ , and  $N_z$ , represent the number of lattice cells along the  $x$ ,  $y$ , and  $z$ -directions for the FDTD algorithm.  $N_e$ ,  $N_c$ , and  $N_n$  represent the number of edges, cells, and nodes in the two-dimensional unstructured meshes used by the PGY algorithm, and  $N_z$  represents the number of cells along the vertical  $z$ -direction.  $N_{e0}$  is the number of edges in the mesh which will require a projection operation for the PGY-algorithm (in regions where the mesh is orthogonal, the projection is not needed). Typically, for quadrilateral meshes,  $N_e \approx 2N_c \approx 2N_n$ . For a uniform mesh, it can be assumed that  $N_c = N_x N_y$ . By exploiting planar symmetry, the memory needed to store the PGY matrices is quite negligible compared to the memory required to store the three-dimensional fields. As a result, the PGY-algorithm requires only ~ 25 % more storage than the FDTD algorithm. However, for problems with complex geometries, the number of quadrilateral cells needed to accurately model the geometry is expected to be much smaller than that required by the FDTD method, and this deficiency can be easily accounted for. The floating point operations required by the PGY algorithm and the FDTD algorithm for an orthogonal mesh of equivalent size are exactly the same. Nonorthogonal meshes introduce additional computations for the PGY-algorithm due to the projection operators.

**Table 2.1**  
**Storage and Floating Point Requirements of Each Algorithm**

Method	Storage	Floating Point Operations/ Time Iteration
FDTD	$6N_x N_y N_z$	$36N_x N_y N_z$
PGY	$[3N_e + N_c + N_n]N_z + 9N_e + 4N_n + 10N_{e_{no}}$	$8(2N_e N_z + N_n N_z + N_c N_z) + 16N_{e_{no}} N_z$

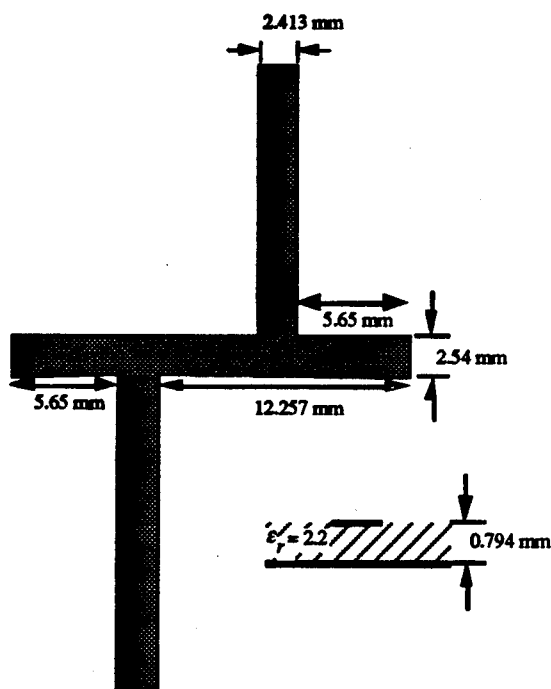


Fig. 2.4 Low pass microstrip filter printed on a dielectric substrate.

Furthermore, the vector lengths of the FDTD algorithm will typically be longer, leading to improved floating point speeds. Thus it is expected that the FDTD algorithm will be faster computationally.

Benchmark comparisons of the two codes are provided here through a simple test case, which is the microstrip low-pass filter illustrated in Fig. 2.4. This problem has been previously modeled using the FDTD algorithm [8], and conforms to a regular grid. To this end, the FDTD grid is defined by an  $80 \times 110 \times 16$  lattice. Unstructured grids were also generated to model this problem for the PGY algorithm. The grids were created to achieve roughly the same level of accuracy as the FDTD algorithm. To this end, the PGY mesh consisted of 8006 quadrilateral cells, and 8160 nodes by 16 cells in the  $z$ -direction. The mesh was generated using SDRC IDEAS, and was partitioned using the RIP partitioning scheme. This task was performed on an HP-workstation.

The microstrip line was excited by a voltage source with a Gaussian pulse wave form, which had a 30 GHz bandwidth. In each case 4000 time iterations were used to reach a converged solution. Initially, keeping the problem size fixed, the problem was executed on a number of processors varying from 1 to 32. The CPU times required to perform the 4000 time iterations are recorded in Table 2.2. Clearly, the FDTD algorithm is the most computationally efficient - especially on the uniprocessor system, where it ran in roughly 1/3 of the time required by the PGY algorithm. This is due to the reduction in floating point operations and the fact that higher floating point speeds are realized by the FDTD algorithm since the vector lengths are much longer.

**Table 2.2**  
**CPU Times Recorded .vs. # of Processors (P)**  
**(Wall Clock Time (seconds) - iPSC/860)**

P	FDTD	PGY
1	2136	6,152
2	1096	3,176
4	588	1,675
8	363	904
16	227	528
32	126	302

**Table 2.3.**  
**Parallel Efficiency .vs. # of Processors (P)**  
**Based on a Fixed Speedup Study**

P	FDTD	PGY
1	100 %	100 %
2	97 %	97 %
4	91 %	92 %
8	74 %	85 %
16	59 %	73 %
32	53 %	64 %

Table 2.3 presents the parallel efficiency of the algorithms based on the fixed speedup study presented in Table 2.2. Interestingly, the FDTD algorithm only records a speedup of 53 % over 32 processors. This is somewhat deceiving, however, since the MFLOPS rate of each processor has been reduced by 64 % due to the shorter vector lengths! If we scale the computational time by this amount, the efficiency would be 83 % (i.e., a speedup of 26.5 over 32 processors). This is quite good, as expected for this algorithm. Nevertheless, there is degradation in the efficiency due to the required interprocessor communication, as well as slight load imbalances and redundant computation. The PGY-algorithm realizes a 64 % parallel efficiency (i.e., a speedup of 20.5 over 32 processors). Here, additional efficiency is principally lost due to load imbalances and interprocessor communication.

It is also instructive to measure the scaled speedup of the algorithms. Specifically, rather than keeping the problem size constant and increasing the number of processors, a scaled speedup study increases the problem size with the number of processors. This study was done on the 512-node Intel Delta. Each node of the Intel Delta also hosts a 40 MHz i860 RISC processor, with only 12 Mb of RAM. Thus the same floating point speeds as the iPSC/860 are realized. Furthermore, the same code developed on the iPSC/860 was directly ported to the Delta. Table 2.4 illustrates the CPU time per time iteration required by each of the algorithms as the problem size is scaled with

**Table 2.4.**  
**Scaled Speedup**  
**CPU seconds / Time Iteration .vs. # of Processors (P)**  
**(Wall Clock Time (seconds) - Intel Delta)**

P	FTD	PGY
1	.532 s	1.53 s
8	.565 s	1.57 s
16	.573 s	1.64 s
32	.574 s	1.65 s
64	.574 s	1.66 s
128	.574 s	1.66 s
256	.575 s	-

the number of processors. Here the problem size is scaled by increasing the mesh size in the transverse directions. It is noticed that the algorithms scale extremely well, and excellent parallel efficiencies are observed. Slight jumps are realized as the problem is scaled beyond the uniprocessor system due to the introduction of interprocessor communication and serial computation. Nevertheless, it can be concluded that the CPU time required for a problem of size  $N$  on 1 processor will execute in roughly the same amount of time as a problem of size  $N \cdot P$  on  $P$  processors. The caveat is that as  $N$  is increased, the total number of time iterations needed to reach a steady state will grow roughly as  $O(\sqrt{N})$ .

A second problem is presented to illustrate the effects of load balancing on the PGY algorithm. To this end, a cylindrical via through a ground plane coupling two  $50 \Omega$  microstrip lines is presented. This is illustrated in Fig. 2.5. The via was analyzed on a 32-node iPSC/860. The two-dimensional mesh modeling the via consisted of 4867 quadrilateral cells. The three-dimensional mesh was 40 cells high along the vertical direction. The mesh was spatially decomposed using both the RIP and the Greedy algorithms. The results of the decompositions are illustrated in Table 2.5. The full simulation required 4000 time iterations. The CPU times required to perform the simulation versus the number of processors are illustrated in Table 2.6, comparing the times that resulted from using the RIP and the Greedy algorithms. Clearly, the Greedy algorithm results in improved CPU times. Figure 2.6 illustrates the speedups of the parallel algorithm, again based on the RIP and Greedy decompositions. The speedup here is defined as being the ratio of the CPU time required to execute the problem on  $P$  processors to that required by a single processor. This is also compared to the ideal case of a linear speedup. Excellent speedups are observed over the 32 processors. Finally, the magnitude of the S-parameters are illustrated in Fig. 2.7. These results compare very well with the measured results presented in [9].

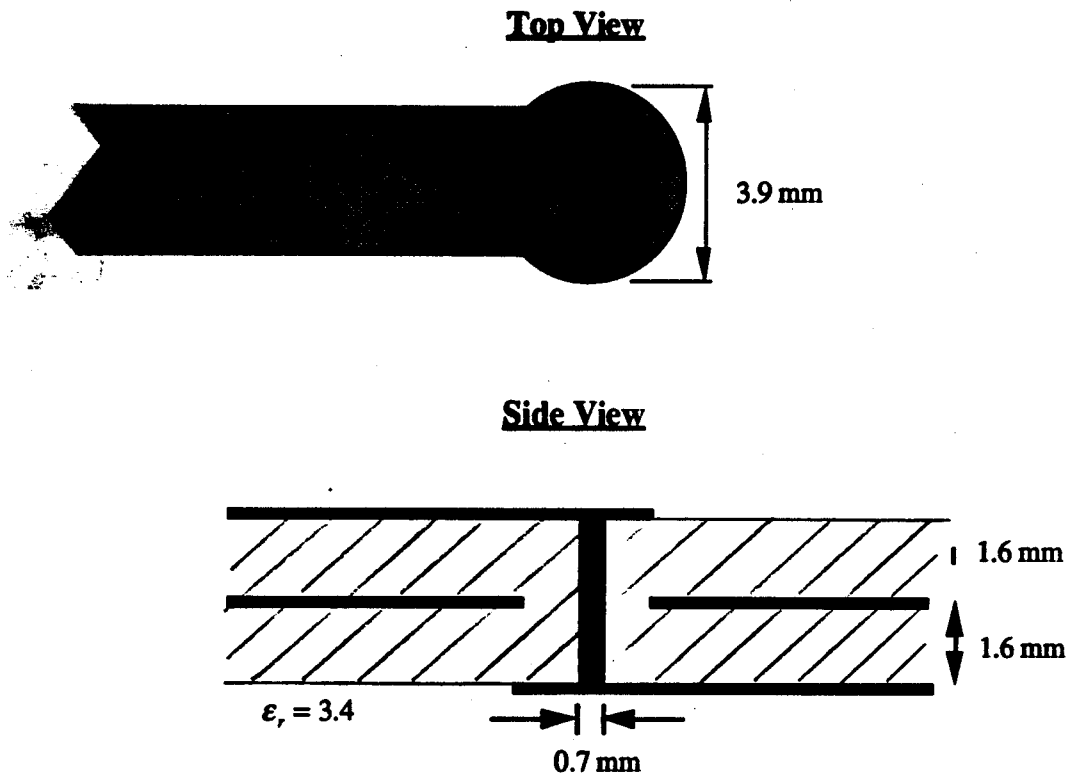


Fig. 2.5 Geometry of a cylindrical via through a PEC ground plane.

**Table 2.5.**  
**Load Balance of the RIP and Greedy Algorithms**

P	RIP		Greedy	
	$N_{c_{max}} : N_{c_{min}}$	$N_{n_{max}} : N_{n_{min}}$	$N_{c_{max}} : N_{c_{min}}$	$N_{n_{max}} : N_{n_{min}}$
1	4867 : 4867	4988 : 4988	4867 : 4867	4988 : 4988
2	2542 : 2325	2629 : 2414	2434 : 2433	2541 : 2541
4	1353 : 1142	1421 : 1210	1217 : 1216	1313 : 1289
8	661 : 571	743 : 621	609 : 608	670 : 662
16	374 : 284	421 : 322	319 : 289	384 : 341
32	203 : 131	236 : 151	153 : 151	190 : 177

**Table 2.6**  
**CPU Times Recorded .vs. # of Processors (P) on iPSC/860**  
**for the Microstrip Via (4000 time iterations)**

P	RIP	Greedy
1	7936.0	7936.0
2	4224.0	4144.0
4	2406.0	2219.0
8	1301.0	1216.0
16	815.00	769.00
32	520.00	384.00

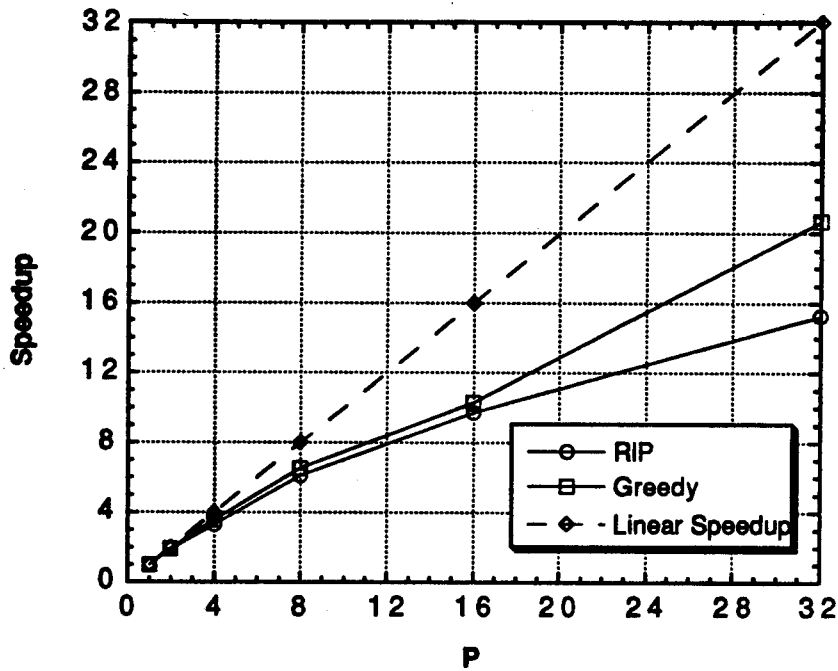


Fig. 2.6 Magnitude of the S-parameters for the cylindrical via through a ground plane computed using the planar generalized Yee-algorithm.

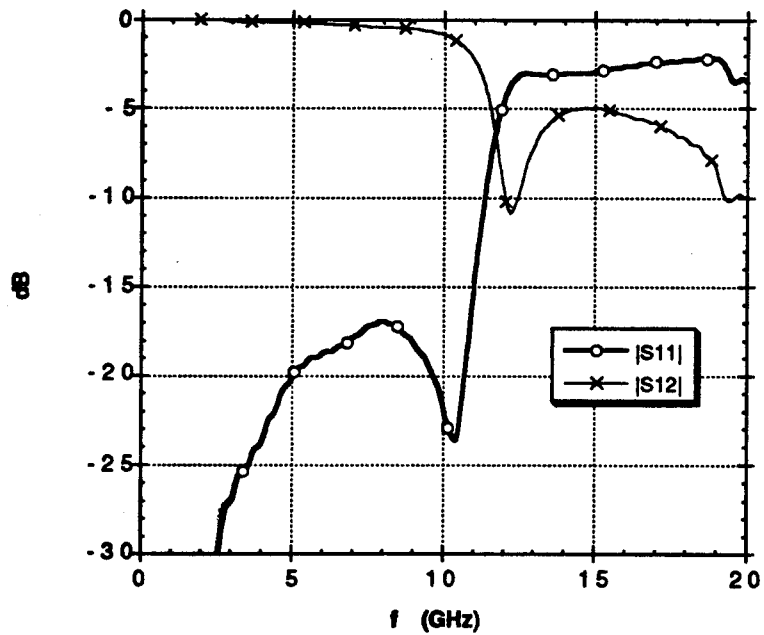


Fig. 2.7 Magnitude of the S-parameters for the cylindrical via through a ground plane computed using the planar generalized Yee-algorithm.

### 2.2.3 References

- [1] A. Taflove and K. Umashankar, "Finite-difference time-domain (FDTD) modeling of electromagnetic wave scattering and interaction problems," *IEEE Antennas and Propagation Magazine*, vol. 30, pp. 5-20, April 1988.
- [2] S. Gedney and F. Lansing, "A Generalized Yee-Algorithm For the Analysis of Three-Dimensional Microwave Circuit Devices with Planar Symmetry," *IEEE Transactions on Microwave Theory and Techniques*, vol. pp. submitted for review 1994.
- [3] S. Gedney and F. Lansing, "A Parallel Planar Generalized Yee-Algorithm For the Analysis of Microwave Circuit Devices," *International Journal for Numerical Modeling (Electronic Networks, Devices and Fields)*, vol. pp. submitted for review August 1994.
- [4] S. Gedney, F. Lansing and D. Rascoe, "A generalized Yee-algorithm for the analysis of MMIC devices," *IEEE Transactions on Microwave Theory and Techniques*, accepted for publication.
- [5] B. Nour-Omid, A. Raefsky and G. Lyzenga, "Solving finite element equations on concurrent computers," in *Symposium on Parallel Computation and their Impact on Mechanics*. Boston: 1987.
- [6] C. Farhat and M. Lesoinne, "Automatic partitioning of unstructured meshes for the parallel solution of problems in computational mechanics," *International Journal on Numerical Methods in Engineering*, vol. 36, pp. 745-764, 1993.
- [7] V. Betz and R. Mittra, "Comparison and evaluation of boundary conditions for the absorption of guided waves in an FDTD simulation," *IEEE Microwave and Guided Wave Letters*, vol. 2, pp. 499-401, December 1992.
- [8] D. Sheen, S. Ali, M. Abouzahra and J. A. Kong, "Application of the three-dimensional finite-difference time-domain method to the analysis of planar microstrip circuits," *IEEE Transactions on Microwave Theory and Techniques*, vol. 38, pp. 849-856, July 1990.
- [9] P. Harms, J.-F. Lee and R. Mittra, "Characterizing the cylindrical via discontinuity," *IEEE Transactions on Microwave Theory and Techniques*, vol. 41, pp. 153-156, January 1993.

## 2.3. ELECTROMAGNETIC PROPERTIES OF MATERIALS – K. W. WHITES

The emphasis of this research is on the computation of the effective constitutive parameters for synthetic chiral materials composed of (lossy) inclusions distributed in a (lossy) host, i.e. suspension, material. The “synthetic” attribute arises since the frequency spectrum under consideration is the microwave region where only man-made chiral materials are known to exist.

The basis for computation of these material parameters is a new methodology developed by the author and involves two basic components. The first is purely numerical and involves a Monte-Carlo method to compute the averaged scattering by a randomly distributed ensemble of inclusions which are constrained to always lie within a free-space volume of canonical shape. In this work, a spherical region is used. This averaging process is continued until convergence is obtained in the far-scattered fields. The second component is a mixture of analytical and numerical methods. The analytical part is to obtain a solution for the far-scattered fields of the canonically-shaped volume with constitutive equations of a presumed form. That is, a continuum model is applied. The numerical part is to match the scattered fields computed from the Monte-Carlo technique with those from the continuum model by varying the constitutive parameters. This is a difficult task due to the nonlinear behavior of the fields as a function of the constitutive parameters. This technique fully accounts for all mutual interactions between inclusions as well as self-interactions – no analytical simplifying models are used.

In the physical application of these artificial materials, the handed inclusions will likely be suspended in a host having dielectric and/or magnetic properties different than those of free space. Therefore, quantification of the interaction between the inclusions and their host as well as the effects on the macroscopic parameters are of utmost importance. In the following section, the numerical methodology for computing these effective constitutive parameters will be outlined with emphasis on the wire-class inclusion geometry. Using this technique, the host material effects on the macroscopic constitutive parameters will be shown for both lossless and lossy host materials.

### 2.3.1 Solution Methodology

The composite chiral materials under investigation in this research effort are composed of many thin-wire helices which are randomly oriented and distributed within a host which is assumed to be simple, homogeneous and, perhaps, lossy in the sense that both  $\epsilon_r$  and  $\mu_r$  are imaginary. The constitutive model chosen to describe this “artificial” material is the Drude, Born, Federov form

$$\begin{aligned}\bar{D} &= \epsilon\bar{E} + \epsilon\beta\nabla \times \bar{E} \\ \bar{B} &= \mu\bar{H} + \mu\beta\nabla \times \bar{H}\end{aligned}\tag{3.1}$$

The computation of the effective constitutive parameters for a composite material is a non-trivial task due to the complex nature of this structure. As described in [1] for a free-space host and

lossless inclusions, this difficulty can be overcome by applying a Monte-Carlo numerical solution together with an analytical solution for the scattering by a chiral material sphere. This technique is inherently numerical in nature and is computationally intensive. However, the effective constitutive parameters in (3.1) can be quantified for any thin-wire shaped inclusion.

All of the inclusion shapes to be analyzed in this summary are composed thin wires, such as a helix. Using the Resistive Tube Boundary Condition (RTBC) [2], an accurate and numerically efficient simulation for material wires can be obtained using a modified electric field integral equation (EFIE) for the vector current  $\bar{I}$ . Assuming that the length of the wire inclusion is much greater than the diameter of the wire, the EFIE is

$$\hat{t} \cdot \bar{E}^i = \frac{R_s}{2\pi b} \hat{t} \cdot \bar{I}(\bar{r}) + jk\eta \hat{t} \cdot \bar{A}(\bar{r}) + \hat{t} \cdot \nabla \Phi_e(\bar{r}) \quad (3.2)$$

where  $\hat{t}$  is a unit tangent vector at any point on all inclusions and the superscript  $i$  indicates the incident electric field assuming an  $e^{j\omega t}$  time dependence. In (3.2),

$$\bar{A}(\bar{r}) = \bar{I}(\bar{r}') * G_{TW}^s(\bar{r}|\bar{r}') \quad \text{and} \quad \Phi_e(\bar{r}) = \frac{\rho_l(\bar{r}')}{\epsilon} * G_{TW}^s(\bar{r}|\bar{r}') \quad (3.3,3.4)$$

where the current and line charge are convolved with the smooth, thin-wire kernel

$$G_{TW}^s(\bar{r}|\bar{r}') = \frac{e^{-jkR_s}}{4\pi R_s} \quad (3.5)$$

and  $R_s$  is taken as the distance from a point on the axis of any wire (source point) to another point on the surface of any wire (observation point). The complex surface resistivity  $R_s$  in (3.2) is given as [2]

$$R_s = -j\eta_d \left[ \frac{J_1(k_d a)}{J_0(k_d a)} - \frac{\eta_d J_1(ka)}{\eta_0 J_0(ka)} \right]^{-1} \quad (3.6)$$

A moment method (MM) solution is formulated following the work of Glisson and Wilton [3] where the current on the wires is expanded in a set of  $N$  piece-wise triangular basis functions with amplitudes  $\alpha_n$  as

$$\bar{I} \approx \sum_{n=1}^N \alpha_n \left[ \frac{\bar{t}_n^+}{l_n^+} - \frac{\bar{t}_n^-}{l_n^-} \right] \quad (3.7)$$

with the definitions of the quantities in (3.7) shown in Figure 3.1. The resulting discretized integro-differential equation is tested with  $N$  piece-wise constant functions, each extending from the centroid of one segment to the centroid of an adjacent segment (contour  $C_m$  as shown in Figure 3.1), to form the  $N$ -by- $N$  constant coefficient matrix equation

$$[V_m] = [Z_{mn}] [\alpha_n] \quad (3.8)$$

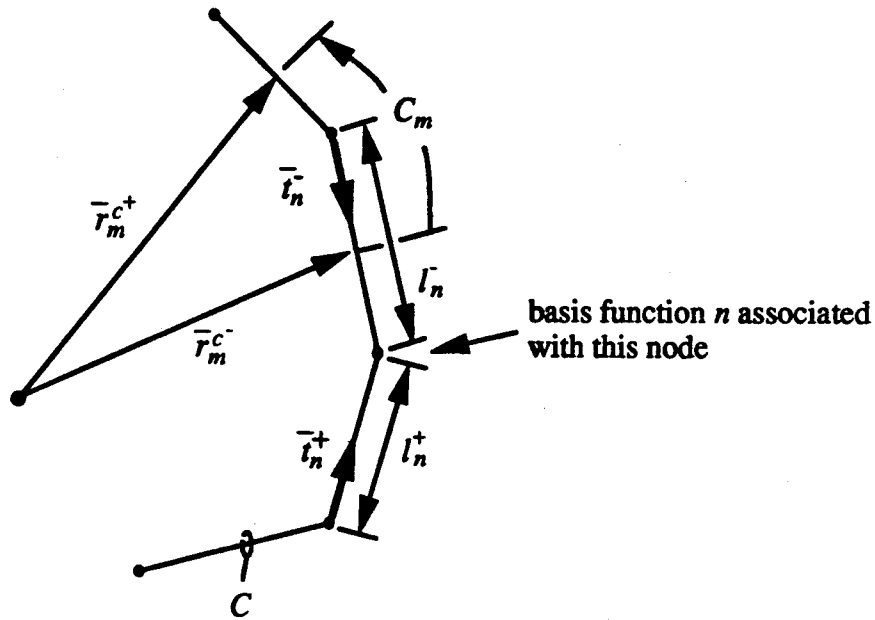


Fig. 3.1. Geometry relevant to the numerical scattering solution for thin-wire structures.

$$\text{where } V_m = \int_{c_m} \hat{t}(\bar{r}) \cdot \bar{E}^i(\bar{r}) dl \text{ and } Z_{mn} = jk\eta \int_{c_m} \hat{t}(\bar{r}) \cdot \bar{A}(\bar{r}) dl + \Phi_e(\bar{r}_m^{c+}) - \Phi_e(\bar{r}_m^{c-}) \quad (3.9)$$

The second step in the application of this technique is to compute the Monte-Carlo averaged scattered fields for an ensemble of thin-wire inclusions. For a particular distribution of thin-wire objects, the far-scattered fields can be found from the Fourier transform of the vector induced current  $\bar{I}$ , for  $i = \theta, \phi$ , as

$$E_i^s(\theta, \phi) \sim -jk\eta g(r) \hat{i} \cdot \{ \mathcal{F}[\bar{I}(\bar{r}')] \} \quad \text{where } k = \omega \sqrt{\mu_{\text{host}} \epsilon_{\text{host}}}, \eta = \sqrt{\mu_{\text{host}} / \epsilon_{\text{host}}} \quad (3.10)$$

$$\equiv g(r) E_i^{\text{scat}}(\theta, \phi) \quad \text{with}$$

$$g(r) = \frac{e^{-jk r}}{4\pi r} \quad \text{and} \quad \mathcal{F}[\bar{I}(\bar{r}')] = \int_{\text{wires}} \bar{I}(\bar{r}') e^{j\bar{k} \cdot \bar{r}'} dl' \quad (3.11)$$

In (3.10), it is presumed that the currents have been numerically computed using the formulation discussed above. Since a *material* necessarily implies a very large number of small inclusions, a “brute force” numerical solution would be cost prohibitive.

To overcome this serious constraint, a Monte-Carlo method is applied where the averaged, far-scattered fields are computed for a relatively small number of inclusions using the “random redistribution algorithm” of [1]. With this method, a plane wave is assumed incident at some fixed angle and the far-scattered electric fields are repeatedly computed using (3.10) for many different randomly computed arrangements of the inclusions. During each iteration, the inclusions are constrained to always lie within an imaginary spherical region, for reasons to be discussed below. Using all of these far-scattered fields, an arithmetic mean is computed at each angle of observation.

The second, and final, step in computing the effective constitutive parameters for these composite chiral materials is to compare the Monte-Carlo averaged scattered fields with those computed analytically for a chiral material sphere. Such an analytical solution was obtained by Bohren [4], and the form of these far-scattered fields is

$$E_{\theta}(\theta, \phi) \sim g(r) \frac{j4\pi}{k} \sum_{n=1}^{\infty} \frac{2n+1}{n(n+1)} \left\{ (a_n \cos \phi - c_n \sin \phi) \frac{P_n^{(1)}}{\sin \theta} + (b_n \cos \phi + d_n \sin \phi) P_n^{(1)'} \right\} \\ \equiv g(r) E_{\theta}^{\text{comp}}(\theta, \phi) \quad (3.12)$$

$$E_{\phi}(\theta, \phi) \sim g(r) \frac{4\pi}{jk} \sum_{n=1}^{\infty} \frac{2n+1}{n(n+1)} \left\{ (a_n \sin \phi + c_n \cos \phi) P_n^{(1)'} + (b_n \sin \phi - d_n \cos \phi) \frac{P_n^{(1)}}{\sin \theta} \right\} \\ \equiv g(r) E_{\phi}^{\text{comp}}(\theta, \phi) \quad (3.13)$$

where  $P_n^{(1)} = P_n^{(1)}(\cos \theta)$  is the associated Legendre polynomial of the first kind, and  $P_n^{(1)'} = \frac{dP_n^{(1)}}{d\theta}$ .

In (3.12) and (3.13) it is assumed that the plane wave is incident in the z-direction with the electric field polarized parallel to the x-axis. Therefore, the incident field in the numerical solution for (3.10) will also have this restriction.

An analytical computation of the effective constitutive parameters obtained by equating the "measured" scattered fields of (3.10) to the "computed" fields of (3.12) and (3.13) is extremely complicated due to the nonlinear dependence. It has been found that the method of simulated annealing is a cost efficient and highly accurate method for finding these material constants [1]. Using this approach a energy function,  $E$ , is defined as the difference between the measured and computed scattered fields at a discrete list of  $J$  observation angles  $(\theta_j, \phi_j)$

$$E(\epsilon, \mu, \beta) \equiv \frac{1}{J \left( |E_{\theta}^{\text{meas}}|^2 + |E_{\phi}^{\text{meas}}|^2 \right)} \sum_{j=1}^J \left\{ \left| E_{\theta}^{\text{comp}}(\theta_j, \phi_j) - E_{\theta}^{\text{meas}}(\theta_j, \phi_j) \right|^2 + \right. \\ \left. \left| E_{\phi}^{\text{comp}}(\theta_j, \phi_j) - E_{\phi}^{\text{meas}}(\theta_j, \phi_j) \right|^2 \right\} \quad (3.14)$$

and subsequently minimized to yield the effective constitutive parameters. By the uniqueness theorem, this set of resulting values will be unique [1].

### 2.3.2 Results

#### 2.3.2.a Partial Verification of the Material Model Method

As a partial verification of the accuracy of the numerical codes and the robustness of the algorithms used in the Monte-Carlo method for numerically modeling artificial materials, a test problem composed of a cloud of pec rods (shown in Figure 3.2) will be analyzed. Following the development in [5], an analytical approximation for the electric polarizability of a single pec rod,

$\alpha_c^0$ , can be determined by approximating the rod as a truncated biconical structure with a radius which varies as a function of distance from the centroid of the bicone. For a rod of length  $2L$  and radius  $b$  [5]

$$\alpha_c^0 = \frac{4\pi\epsilon L^3}{3\ln(2L/b)} \left[ 1 + \frac{1}{3\ln(2L/b)} \right]. \quad (3.15)$$

The end effects have been ignored in (3.15) which, assuming thin rods, is a reasonable approximation. However, for increasingly large radii there is additional charge accumulation on the endcaps of the rod which would tend to increase  $\alpha_c^0$ .

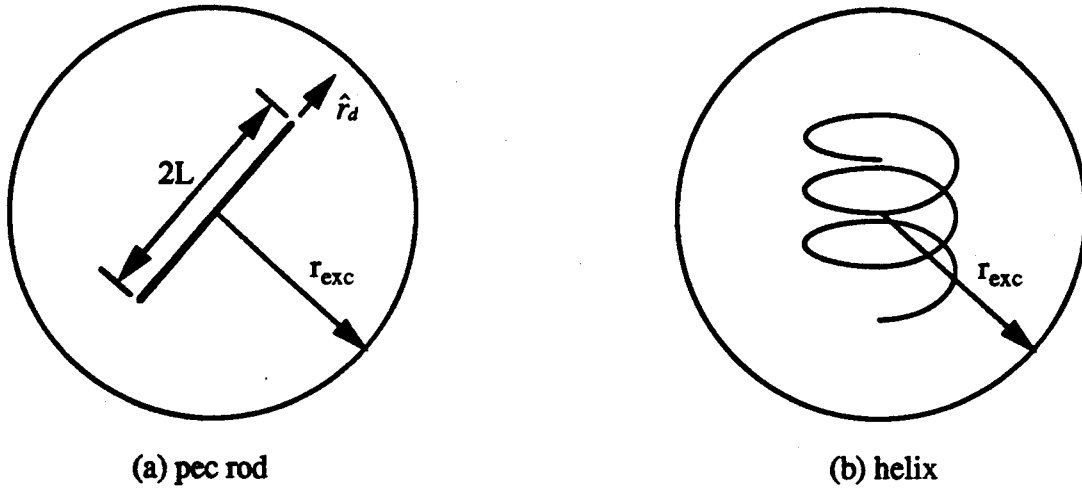


Fig. 3.2. Geometry of the thin-wire inclusion shapes. In the Monte-Carlo simulations, an imaginary exclusion sphere of radius  $r_{exc}$  is assumed about each inclusion.

With an incident electric field linearly polarized parallel to a small, isolated pec rod, the induced electric dipole moment  $\bar{p}$  in terms of the electric field is given as

$$\bar{p} = \alpha_c^0 (\hat{r}_d \cdot \bar{E}^{inc}) \hat{r}_d \quad (3.16)$$

for the rod axis pointing in the  $\hat{r}_d$  direction. Using (3.15), an effective media characterization for a cloud of randomly distributed, non-interacting pec rods can easily be computed. The traditional definition of the electric dipole moment density in terms of  $N$  (the number density), the spatial average of the induced electric dipole moment and the electric susceptibility is [6]

$$\bar{P} = N \langle \bar{p} \rangle = \epsilon_0 \chi_c \bar{E} \quad (3.17)$$

where  $\bar{p}$  is given in (3.16). Since all mutual interaction of the rods is ignored, the spatial average in (3.17) can alternatively be computed by averaging (3.16) over all orientation angles of a single rod as

$$\langle \bar{p} \rangle = \frac{\iint f(\theta, \phi) \bar{p} d\theta d\phi}{\iint f(\theta, \phi) d\theta d\phi} \quad (3.18)$$

where  $f$  is some weighting function and  $\theta$  and  $\phi$  are local angle variables. Choosing  $f = 1$  and noting that simply flipping the rod does not alter  $\bar{p}$ , then

$$\langle \bar{p} \rangle = \frac{1}{\pi^2} \int_0^{2\pi} \int_0^{\pi/2} \bar{p} d\theta d\phi = \frac{\alpha_e^0}{2} \bar{E}^{inc} \quad (3.19)$$

From (3.15), (3.16) and (3.19), the average polarizability,  $\alpha_e$ , and effective electric susceptibility,  $\chi_e^{eff}$ , for a cloud of  $N$  non-interacting pec rods per unit volume are then

$$\alpha_e = \frac{\alpha_e^0}{2} \quad \text{and} \quad \chi_e^{eff} = \frac{N\alpha_e}{\epsilon_0} \quad (3.20)$$

A comparison between the approximate analytical treatment of the Rayleigh scattering by a cloud of randomly distributed pec rods and the numerical solution method of this paper is given in Figure 3.3. The rods all have dimensions  $2L = 1.5$  and  $b = 0.015$  mm and are randomly oriented and distributed within a free-space spherical volume of radius 20 mm at a frequency of 1 GHz. The analytical results use (3.20) while the numerical solutions are computed using the random redistribution schedule of Section II. Also shown in Figure 3.3 is the numerical results when all mutual interactions between inclusions are ignored. In this case the separation between rods is no less than  $r_{exc} = 4L$ , while for the full-wave solution  $r_{exc} = 2L$ . The fact that the full-wave results lie between the other two is primarily due to a smaller basis function density in the full-wave results.

### 2.3.2.b Free space host, lossless inclusions results

Using the methodology developed in the previous section, the effective chiral material parameters for a collection of pec helical inclusions were computed and are shown in Figure 3.4 for the frequency range 1 to 13 GHz. The three-turn helices have dimensions  $a = P = 0.5$  mm and  $b = 0.05$  mm while the computation of the effective constitutive parameters was done using the random redistribution Monte-Carlo algorithm for a collection of 40 helices in a free-space volume with  $r_{sph} = 4.9$  mm. The number of Monte-Carlo iterations required for convergence varied from 10-20 at low frequencies where the mutual coupling was small, to 40-60 at higher frequencies where the mutual coupling is increasing.

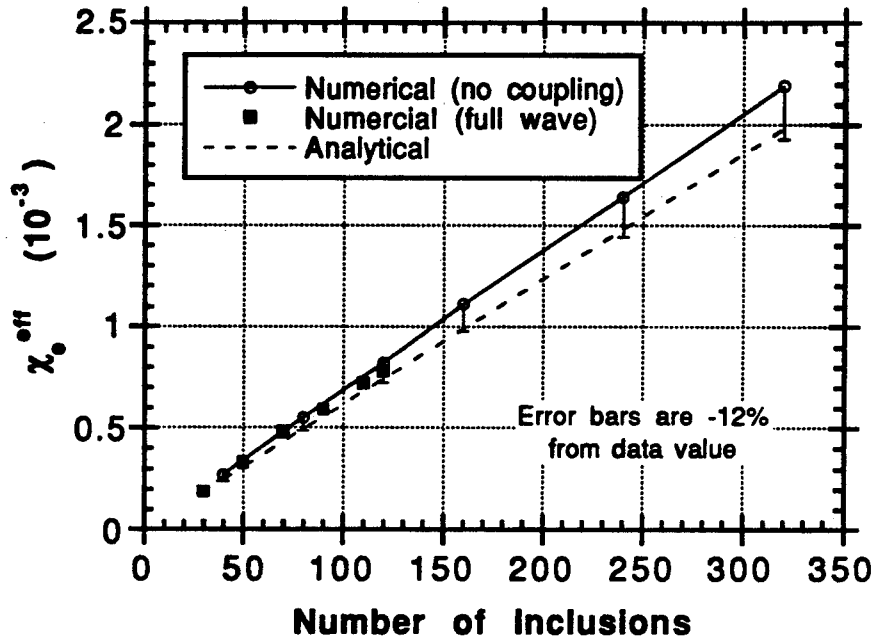


Fig. 3.3. Effective media electric susceptibility comparison for a cloud of pec rods suspended in a free-space spherical volume of radius  $r_{sph} = 20\text{mm}$ .

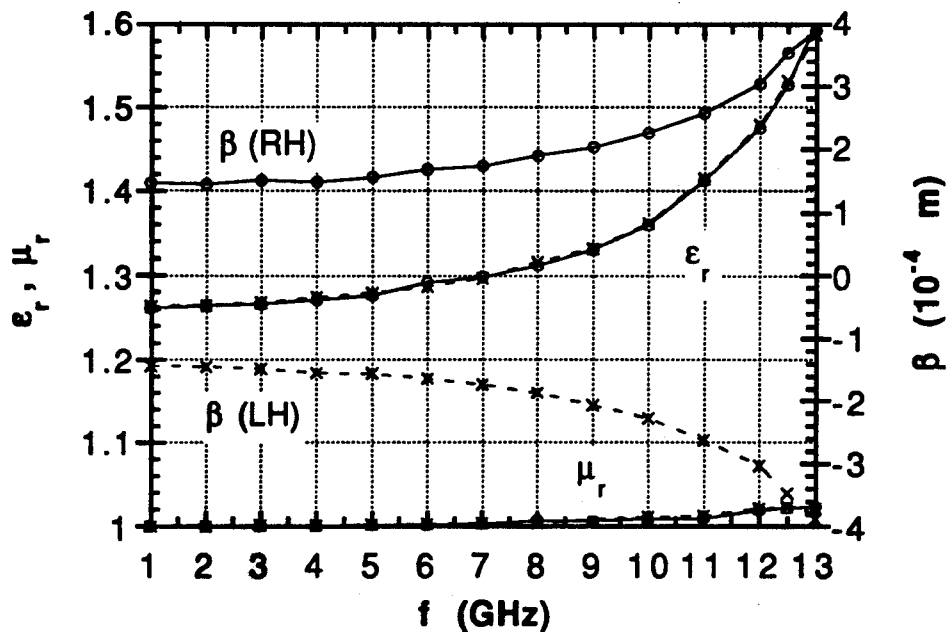


Fig. 3.4. Effective chiral media parameters for a random distribution of three-turn pec helices having  $a = P = 0.5$ ,  $b = 0.05$  mm and  $N = 8.117 \cdot 10^7/\text{m}^3$ . Forty helices suspended in a free-space spherical region with  $r_{sph} = 4.9\text{mm}$  were used in the simulation. The symbols 'o' and 'x' designate right- and left-handed helices, respectively.

A 32-node Intel iPSC<sup>®</sup>/860 hypercube, together with the Intel ProSolver<sup>™</sup>-DES library, was used to generate most of the data in this report. For each data point shown in Figure 3.4, approximately 8 node-hours was required for each Monte-Carlo iteration (fill and solve for 40 helices and 60 basis functions per helix) plus an additional 0.5 node-hours for the SA determination of the effective constitutive parameters. The integrals appearing in (3.9) were computed numerically using a Romberg integration technique which results in most of the 8 node-hours being spent filling the Z-matrix of (3.9).

Returning to Figure 3.4, a number of important observations can be made which strengthen the argument for the accuracy of these effective material parameters. The first observation is that both  $\epsilon$  and  $\mu$  are virtually identical, at the same frequency, for either the right- or left-handed inclusions while  $\beta$  changes sign. These results are consistent with the invariant scalar nature of  $\epsilon$  and  $\mu$  and the pseudoscalar nature of  $\beta$  [7]. Upon a spatial inversion of the coordinate system, the field vectors  $\bar{E}$  and  $\bar{D}$  behave as true vectors while  $\bar{B}$  and  $\bar{H}$  transform as pseudovectors [8]. Assuming form invariance of (3.1), then  $\epsilon$  and  $\mu$  must remain unchanged after a spatial reflection (and a random material), while  $\beta$  must change sign.

The second observation from the results in Figure 3.4 is that the magnitude of  $\beta$  is of order  $10^{-4}$  m while the magnitude of  $\mu$  is approximately one over the entire frequency range shown. This same order of magnitude for  $\beta$  was inferred from experimental data as communicated in [9], while in [10]  $\beta$  and  $\mu$  values were obtained, using a simplifying analytical model, near those reported in this work. It is noted from the data in Figure 3.4 that  $|k\beta| < 1$ , where  $k \equiv \omega\sqrt{\mu\epsilon}$ , as required for physically realizable chiral materials [9, 11].

While the above two sets of observations lend credence to the reasonableness of the effective constitutive parameters for the artificial chiral material, it is also important to note their phenomenological behavior as a function of frequency. Below approximately 4 GHz, the parameters are relatively constant and  $\beta$  remains nonzero. However, even with this sizable value of  $\beta$ , the optical rotatory dispersion (ORD) for a path length  $d$  within the chiral material

$$\text{ORD} \equiv \frac{\phi_r}{d} = -\frac{18}{5\pi} \frac{k^2\beta}{1-k^2\beta^2} \quad (^\circ/\text{cm}) \quad , \quad (3.21)$$

is vanishingly small as shown in Figure 3.5. This is consistent with the notion that the electromagnetic effects of chirality vanish at zero frequency [7, 12]. In the DBF equations (3.1), this can occur even for non-vanishing chirality factor  $\beta$ . In fact, it can be shown using a Fourier transform approach as in [8, p. 306] that  $\beta$  is an even function of frequency for lossless materials and hence may not vanish at dc. This is in contrast to other forms of the constitutive equations, such as the Lindell-Sihvola form [12, 13], which necessarily require the chirality parameter to vanish at zero frequency [12].

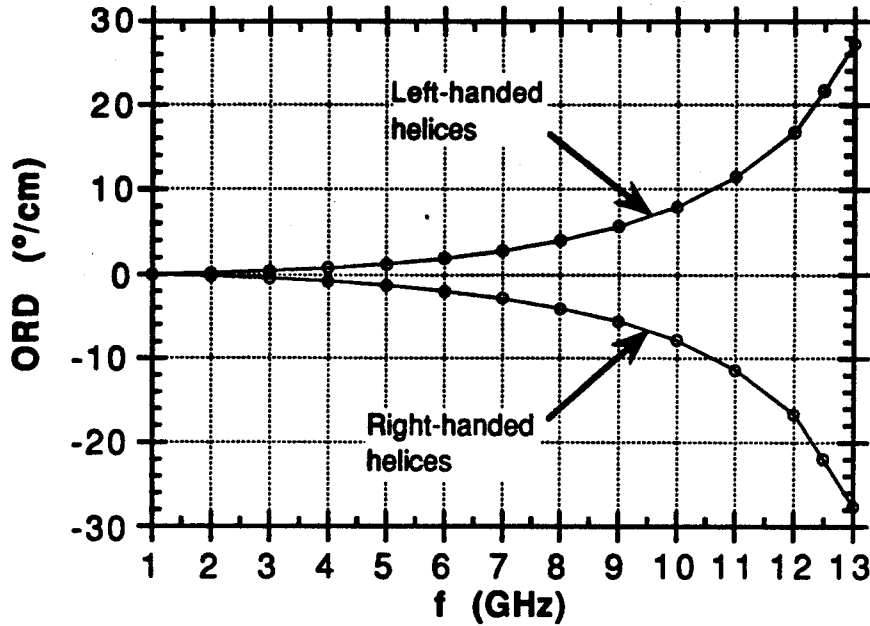


Fig. 3.5. Optical rotary dispersion (ORD) for the artificial chiral material described in Figure 3.4.

### 2.3.2.c Lossless host and inclusions results

Shown in Figure 3.6 are the effective material parameters when the host is a lossless dielectric having  $\epsilon_{r,host} = 2$  with inclusions of three-turn, right-handed helices having  $a = \text{radius} = 0.6\text{mm}$ ,  $P = \text{pitch} = 0.3\text{mm}$  and  $b = \text{wire radius} = 0.05\text{mm}$ . For these results, 40 helices are suspended in a spherical volume of radius  $r_{sph} = 5\text{mm}$  yielding a number density  $N = 7.6394 \cdot 10^7 \text{ m}^{-3}$  and a metal volume concentration of 0.68073%. The general behavior of this material as a function of frequency is similar to that seen for the free-space host. As expected, the resonant frequency of the inclusion is reduced by the factor  $\sqrt{\epsilon_{r,host}}$ . For frequencies much lower than this resonant frequency, it is noted that a lossless dielectric host produces an increase in the effective relative permittivity proportional to the host permittivity while both  $\beta$  and  $\mu_r$  increase only slightly. Hence, the increase in ORD, with respect to a free-space host, at low frequencies and small  $\beta$  is proportional to  $\epsilon_{r,host}$ .

### 2.3.2.d Lossy host, lossless inclusions results

Figure 3.7 shows these material parameters for the wire helices of the same dimensions and number density mentioned above, except with a host having  $\epsilon_{r,host} = 2 - j1$ . A notable, and expected, change in the response of this material, as compared to the lossless one, is the

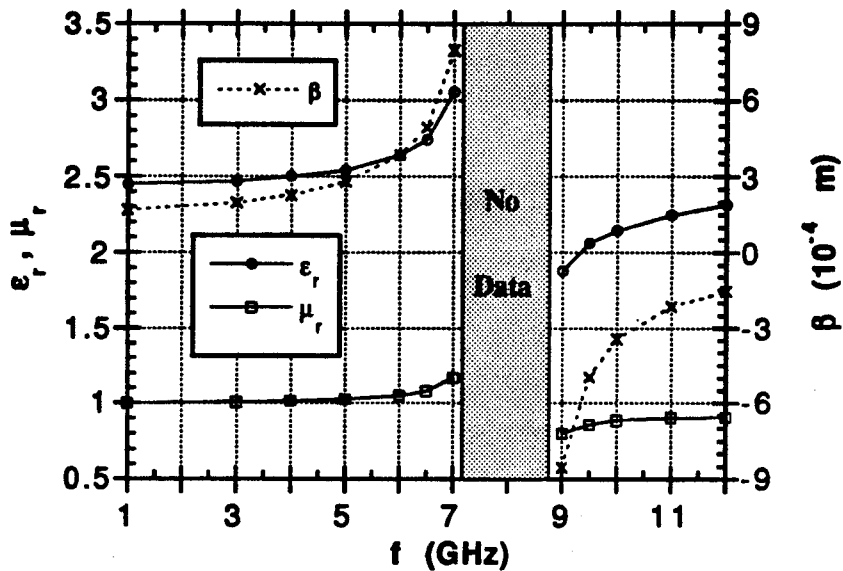


Fig. 3.6. Effective chiral media parameters for a random distribution of three-turn right-handed pec helices having  $a = 0.6$ ,  $P = 0.3$ ,  $b = 0.05$  mm and  $N = 7.6394 \cdot 10^7/m^3$ . Forty helices suspended in a free-space spherical region with  $r_{sph} = 4.9$ mm were used in the simulation. The host material has parameters  $\epsilon_{r,host} = 2$ ,  $\mu_{r,host} = 1$ .

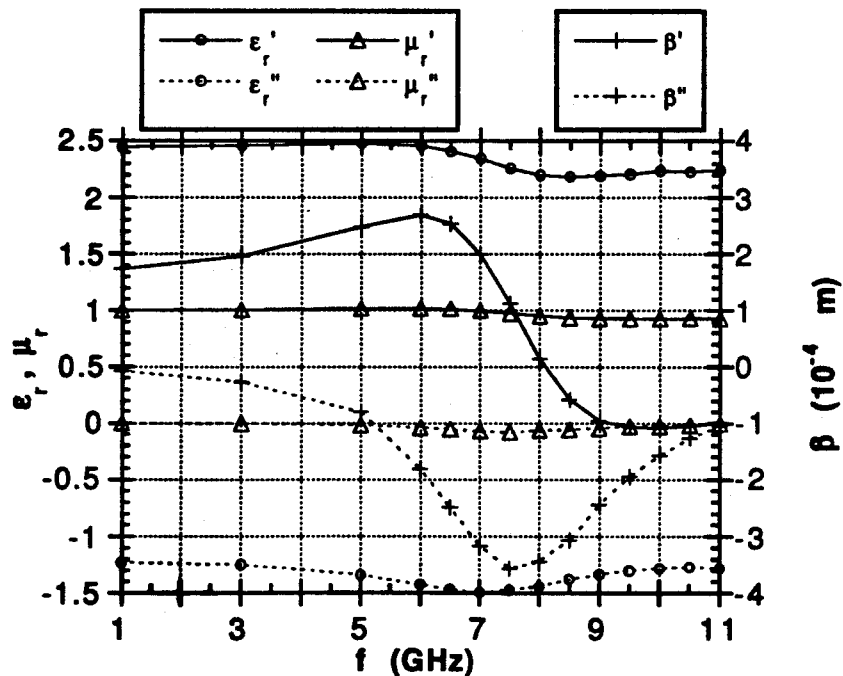


Fig. 3.7. Effective chiral media parameters for a random distribution of three-turn right-handed pec helices with dimension given in Fig. 3.6. The host material has parameters  $\epsilon_{r,host} = 2 - j1$ ,  $\mu_{r,host} = 1$ .

appearance of the absorption band near the  $\lambda/2$  resonance frequency of the helix ( $f \approx 8\text{GHz}$ ). Such behavior has been noted before in connection with composite chiral materials [4]-[6]. Within the absorption band there occurs an “anomalous rotary dispersion” where the polarization tilt angle (not shown) of an emerging plane wave passing through a slab of this material changes sign as a function of frequency. Similar behavior has been measured for chiral composites in the microwave frequency bands [7].

### 2.3.2.e Free-space host, lossy inclusions results

The final data to be presented in this section on materials modeling is for helical inclusions composed of lossy wires, i.e., wires that have finite conductivity. A model which is often used to describe the frequency dispersion in the material parameters is the single-resonance Condon model [13]. Since for the DBF equations (3.1),  $\beta$  is an even function of frequency [1], the “Lorentz-type” frequency dependence can be written as

$$\beta(\omega) = \frac{A}{1 - x^2 + jDx} \quad (3.22)$$

where  $A$  is the amplitude,  $D$  is a damping factor,  $x = \omega/\omega_0$  and  $\omega_0$  is the resonant radian frequency. By defining  $\beta \equiv \beta' + j\beta''$  it can be shown that

$$\beta' = \frac{A(1 - x^2)}{1 + (D^2 - 2)x^2 + x^4} \quad \text{and} \quad \beta'' = -\frac{ADx}{1 + (D^2 - 2)x^2 + x^4} \quad (3.23)$$

The three constants appearing in (3.23) are determined by fitting the curve to the numerically obtained “exact” values for the chirality parameter  $\beta$ .

The effective chirality parameter for a three-turn right-handed helices composed of lossy wires are shown in Figures 3.8 and 3.9. In Figure 3.8,  $\sigma = 10^5\text{S/m}$  while in Figure 3.9,  $\sigma = 10^5\text{ S/m}$ . The symbol-denoted data points were obtained using the numerical methodology outlined in this report together with the iPSC/860. The solid lines are the Lorentz-dispersion modeled results. It is seen that the agreement is quite good thus confirming the frequency dependence of this synthetic chiral materials in the anomalous dispersion bands.

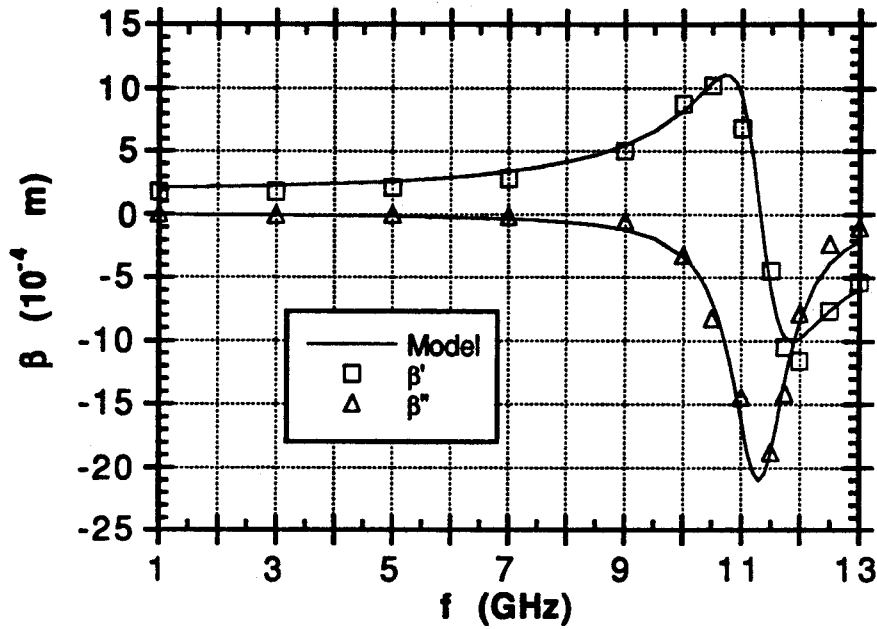


Fig. 3.8. Effective chirality parameter  $\beta$  for a random distribution of three-turn right-handed helices (wire conductivity =  $10^5$  S/m) with dimension given in Fig. 3.6. The host material has parameters  $\epsilon_{r,host} = 1, \mu_{r,host} = 1$ .

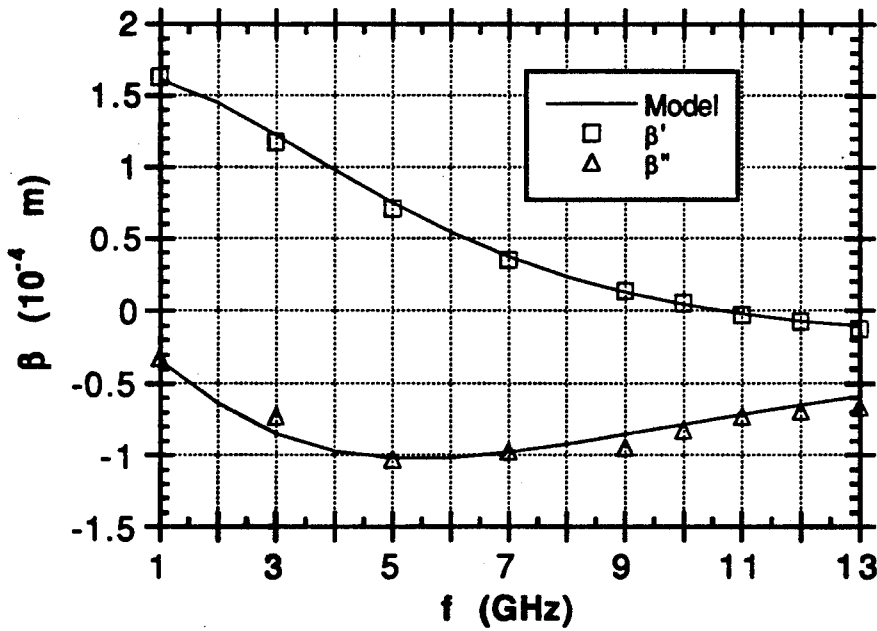


Fig. 3.9. Effective chirality parameter  $\beta$  for a random distribution of three-turn right-handed helices (wire conductivity =  $10^3$  S/m) with dimension given in Fig. 3.6. The host material has parameters  $\epsilon_{r,host} = 1, \mu_{r,host} = 1$ .

### 2.3.3 References

1. K. W. Whites, "Full-wave computation of constitutive parameters for lossless composite chiral materials," *IEEE Trans. Antennas Propagat.*, submitted for publication.
2. K. W. Whites, "A simple scattering model for thin material wires," *Digest of the 1992 IEEE Antennas and Propagation Society International Symposium*, Chicago, IL, pp. 691-694, July, 1992.
3. A. W. Glisson and D. R. Wilton, "Simple and efficient numerical methods for problems of electromagnetic radiation and scattering from surfaces," *IEEE Trans. Antennas Propagat.*, vol. AP-28, no. 5, pp. 593-603, 1980.
4. C. F. Bohren, "Light scattering by an optically active sphere," *Chem. Phys. Lett.*, vol. 29, no. 3, pp. 458-462, 1974.
5. S. A. Schelkunoff and H. T. Friis, *Antennas: Theory and Practice*. New York: John Wiley & Sons, 1952.
6. M. Born and E. Wolf, *Principles of Optics: Electromagnetic Theory of Propagation, Interference and Diffraction of Light*. Oxford, England: Pergamon Press, sixth ed., 1980.
7. A. Lakhtakia, V. K. Varadan and V. V. Varadan, *Time-Harmonic Electromagnetic Fields in Chiral Media*. Berlin: Springer-Verlag, 1989.
8. J. D. Jackson, *Classical Electrodynamics*. New York: John Wiley & Sons, second ed., 1975.
9. V. V. Varadan, Y. Ma and V. K. Varadan, "Effects of chiral microstructure on EM wave propagation in discrete random media," *Radio Sci.*, vol. 24, no. 6, pp. 785-792, 1989.
10. A. J. Bahr and K. R. Clausing, "An approximate model for artificial chiral material," *IEEE Trans. Antennas Propagat.*, submitted for publication.
11. N. Engheta and D. L. Jaggard, "Electromagnetic chirality and its applications," *IEEE Antennas Propagat. Mag.*, vol. 30, no. 5, pp. 6-12, 1988.
12. A. H. Sihvola and I. V. Lindell, "Bi-isotropic constitutive relations," *Microwave Opt. Technol. Lett.*, vol. 4, no. 8, pp. 295-297, 1991.
13. I. V. Lindell, A. H. Sihvola, S. A. Tretyakov and A. J. Viitanen, *Electromagnetic Waves in Chiral and Bi-Isotropic Media*. Boston: Artech House, 1994.

### 3. PUBLICATIONS

#### 3.1 JOURNAL PAPERS PUBLISHED/SUBMITTED

##### 3.1.1 S. Gedney

- [1] Stephen D. Gedney and Umesh Navsariwala, "A comparison of the performance of the finite difference time-domain, finite element time-domain, and planar generalized Yee-algorithms on high performance parallel computers," *International Journal on Numerical Modeling (Electronic Networks, Devices and Fields)*, accepted for publication.
- [2] Stephen D. Gedney and Faiza Lansing, "A parallel planar generalized Yee-algorithm for the analysis of microwave circuit devices," *International Journal on Numerical Modeling (Electronic Networks, Devices and Fields)*, accepted for publication.
- [3] Stephen D. Gedney and Faiza Lansing, "A full-wave analysis of passive monolithic integrated circuit devices using a generalized Yee-algorithm," *IEEE Transactions on Microwave Theory and Techniques*, accepted for publication.
- [4] Stephen D. Gedney and Faiza Lansing, "A generalized Yee-algorithm for the analysis of three-dimensional microwave circuit devices with planar symmetry," submitted to *IEEE Transactions on Microwave Theory and Techniques*.
- [5] Stephen D. Gedney, "Finite-difference time-domain analysis of microwave circuit devices on high performance vector/parallel computers," submitted to *IEEE Transactions on Microwave Theory and Techniques*.

##### 3.1.2 K. Whites

- [1] K. W. Whites, "Full-wave computation of constitutive parameters for lossless composite chiral materials," *IEEE Trans. Antennas Propagat.*, submitted for publication.

#### 3.2 CONFERENCE PAPERS PUBLISHED/PRESENTED

##### 3.2.1 S. Gedney

- [1] Stephen D. Gedney, "A comparison of the performance of finite-difference time-domain, finite element time-domain, and discrete surface integral equation methods on high performance parallel computers," 1994 IEEE Symposium on Antennas and Propagation Digest, Seattle, WA, June 19-24, 1994.
- [2] Stephen D. Gedney and Faiza Lansing, "A parallel discrete surface integral equation method for the analysis of three-dimensional microwave circuit devices with planar symmetry," 1994 IEEE Symposium on Antennas and Propagation Digest, Seattle, WA, June 19-24, 1994.
- [3] Stephen D. Gedney and Umesh Navsariwala, "The analysis of three-dimensional microwave circuits and antennas using a parallel finite element time-domain method," URSI Radio Science Meeting Digest, Seattle, WA, June 19-24, 1994.
- [4] Stephen D. Gedney and Faiza Lansing, "The full wave analysis of microwave devices on the Intel Delta," presented at the Second CSCC Delta Applications Workshop, Concurrent Supercomputing Consortium, Norfolk, VA, March 25-26, 1993.

- [5] Stephen D. Gedney and Faiza Lansing, "Time domain analysis of planar microstrip devices using a generalized Yee-algorithm based on unstructured grids," 1993 Progress In Electromagnetics Research Symposium Proceedings, Pasadena, CA, pg. 561, July 12-16, 1993.
- [6] Stephen D. Gedney and Faiza Lansing, "Full wave analysis of printed microstrip devices using a generalized Yee-algorithm," 1993 IEEE Symposium on Antennas and Propagation Proceedings, Ann Arbor, MI, June 27-July 2, 1993.

### 3.2.2 K. Whites

- [1] K. W. Whites, "Surmounting numerical limitations in the full-wave simulation of chiral materials," *Digest of the 1993 URSI Radio Science International Symposium*, Ann Arbor, MI, pp. 243, June, 1993.
- [2] K. W. Whites, "Host effects on the constitutive parameters for synthetic chiral media," *Proceedings of Chiral'94* (invited), Perigueux, France, pp. 77-82, May, 1994.
- [3] K. W. Whites, "Computation and physical behavior of bi-isotropic material parameters for a class of lossy inclusions," *Digest of the 1994 URSI Radio Science International Symposium*, Seattle, WA, pp. 428, June, 1994.

## 4. SUPPORTING PERSONNEL

No personnel were supported with funds from this grant, only equipment. The personnel directly involved with the research performed with the equipment funded were: Dr. Stephen Gedney, and Dr. Keith Whites, Department of Electrical Engineering, University of Kentucky.

## 5. REPORT OF INVENTIONS

No patents have been filed based on the research performed under this grant.